Magnetotransport behavior of epitaxial graphene inhomogeneously doped by Bi(110) islands

Julian Koch,[1,*] Sergii Sologub,[1,2] Chitran Ghosal,[1] Teresa Tschirner,[3] Atasi Chatterjee,[3] Klaus Pierz,[3] Hans Werner Schumacher,[3] and Christoph Tegenkamp[1,†]

[1]*Institut für Physik, Technische Universtät Chemnitz, Reichenhainerstr. 70, 09126 Chemnitz, Germany*
[2]*Institute of Physics, National Academy of Sciences of Ukraine, Nauki avenue 46, 03028 Kyiv, Ukraine*
[3]*Physikalisch-Technische Bundesanstalt, Bundesallee 100, 38116 Braunschweig, Germany*

(Received 12 February 2024; revised 12 April 2024; accepted 16 May 2024; published 3 June 2024)

The concept of proximity coupling is a promising approach to specifically modify the properties of epitaxial graphene layers. In order to introduce spin-orbit coupling into graphene, we have deposited Bi with an average thickness of up to 3.6 bilayers (BL) on epitaxial monolayer graphene (MLG) on SiC(0001) and perform magnetotransport measurements in magnetic fields up to 4 T. Upon adsorption, epitaxial Bi(110) islands are formed, which change the initial *n*-type doping of MLG locally. The formation of inhomogeneous carrier concentration profiles on MLG results in a positive and linear magnetoresistivity effect with increasing Bi coverage. Along with this, the slope of the Hall resistivity decreases, suggesting a rise of the carrier concentration. However, by extracting the carrier concentration from the Shubnikov–de Haas oscillations, we confirm that the carrier concentration in the uncovered regions remains constant and that the change of the Hall slope is solely an effect of the inhomogeneity. Also, the conductivity of MLG has not changed drastically and even at coverages as high as 2.4 BL the mobility in the noncovered region is reduced by only about 15% of its original value. Moreover, the signatures of weak localization in the magnetoresistivity vanish with increasing Bi coverage, while no signs of weak antilocalization were found at all. Apparently, the proximitized Bi islands induce a well-defined lateral doping profile so that the electrons are not penetrating into the areas of the Bi islands, thus mimicking antidots, but are reflected at their edges. This scattering process seems to be phase breaking, thus suppressing the weak localization effect. Our results show clearly that both the coupling but also the homogeneity at the interface is crucial for proximity coupling.

DOI: 10.1103/PhysRevB.109.235107

I. INTRODUCTION

Graphene is an almost ideal material for use in electronics, due to its unique properties, especially the high charge carrier mobility and the long mean free path of linear dispersed electrons [1]. In order to further tune its transport characteristics and induce properties that are not inherent to it, proximity coupling is a promising approach. One of the desired modifications is a strengthening of graphene's negligible intrinsic spin-orbit coupling (SOC) to improve the control of spin currents and promote the emergence of magnetic quantum states. To date, a number of studies in this direction have already been carried out, in which graphene is brought into contact with suitable materials. Some of these materials are topological insulators [2–4], which produce spin-orbit splitting of up to 80 meV [5]; others are dichalcogenides of transition metals [6]. Adsorption of heavy metal clusters have also proved to be effective. In particular, the adsorption of copper/gold clusters increases the spin-orbit splitting up to 20 meV [7]. Another method is the hydrogenation and fluorination of graphene [8,9] resulting in spin-orbit splitting of 2.5 meV [10].

Bi, adsorbed on graphene, is a promising material for inducing or strengthening SOC. The use of Bi avoids dealing with multielement materials, in particular, complications with achieving a uniform stoichiometry during the growth process. Bi is a heavy semimetal with surface electronic states that are spin-split due to the Rashba effect [11,12]. In addition, there is evidence that Bi is a higher order topological insulator (HOTI) with protected edge states [13]. Thus it is not surprising that the electronic and structural properties of Bi adsorbed on graphene have already attracted the attention of researchers. Ultrathin Bi nanofilms adsorbed on graphene with an average thickness of up to 7 bilayers (BL) were shown to possess a Bi(110) surface termination and corresponding low energy electron diffraction (LEED) patterns reveal three equivalent main Bi(110) domains, characterized by the coincidence of the zigzag direction of Bi(110) with the armchair direction of graphene [14,15]. In addition, each domain has two subdomains rotated by $\pm 2^\circ$ [15,16]. At Bi coverages greater than 7 BL a Bi(111) structure is formed [14]. In addition, scanning tunneling microscopy (STM) studies demonstrate the formation of Bi(110) islands of different heights, which are strongly elongated in the armchair direction of graphene, as well as the formation of triangular Bi(111) islands [14,16,17]. Moreover, the local density of states of Bi(110) islands was found to be layer dependent. In particular, 2 BL thick Bi(110) islands are semiconducting and possess edge states, while thicker films exhibit metallic characteristics [18].

At low magnetic fields the magnetotransport behavior of graphene is governed by weak (anti)localization (WL/WAL).

*julian.koch@physik.tu-chemnitz.de
†christoph.tegenkamp@physik.tu-chemnitz.de

While the SOC in graphene is negligible, it hosts two other types of "spins"—the A/B sublattice related isospin and the K/K′ related valley pseudospin [19,20]. The complex interplay of these two spins results in either WL or WAL depending on the strength of the corresponding scattering mechanisms. However, under most experimental conditions WL is observed [21]. WAL is only observed under the absence of intervalley scattering or in the case of low carrier concentration ($n < 10^{12}$ cm^{-2}) and sufficiently high temperature [21]. Furthermore, in order to take SOC into account, two mechanisms are considered, namely Kane-Mele and Bychkov-Rashba, which are associated with the Elliott-Yafet and the D'yakonov-Perel mechanisms of spin relaxation, respectively [20,22].

We will show that the doping of the graphene due to the Bi islands is highly local resulting in a strongly inhomogeneous distribution of the carrier concentrations across the graphene substrate. In general, an inhomogeneous carrier concentration or mobility leads to a positive contribution to the magnetoresistivity, that is parabolic at low fields ($\mu B \ll 1$) and linear at high fields ($\mu B \gg 1$), as well as a change of the Hall slope, due to the Hall field and the Lorentz force no longer compensating each other locally [23]. The positive contribution to the magnetoresistivity is a result of the interplay of the scattering of the charge carriers in the vicinity of the low conducting regions and diffusive dynamics [24,25].

We focus on magnetotransport experiments in order to quantify the transport characteristics of monolayer graphene covered by Bi(110) islands. From these measurements, we have determined the characteristic scattering times corresponding to different electron scattering mechanisms, as well as the mobility and the concentration of charge carriers. The transport data is correlated with structural data obtained by spot profile analysis LEED (SPA-LEED) and STM.

II. EXPERIMENTAL METHODS

The magnetotransport measurements were performed in ultrahigh vacuum (UHV) at a base pressure of 7×10^{-11} mbar and at a sample temperature of 12 K. A magnetic field up to ±4 T was applied using a superconducting split coil magnet. Two substrates were used in this study, referred to as sample 1 and sample 2 in the following. Both of them were an epitaxial monolayer of graphene (MLG) on a $10 \times 10 \times 0.5$ mm^3 4H-SiC(0001) crystal [nitrogen doped, *n*-type, $\rho = 0.099\ \Omega$cm (sample 1) and $\rho = 2.6 \times 10^{11}\ \Omega$cm (sample 2)], prepared *ex situ* by heating the SiC crystal in an Ar atmosphere. They were degassed inside the UHV chamber at 500 °C in order to remove contaminants such as oxygen. Bi islands were grown *in situ* at a sample temperature of 300 K by evaporation of Bi from a Knudsen cell. The amount was controlled by a quartz crystal microbalance. The deposition rate was 0.23 bilayers [BL, with respect to Bi(110)] per minute. The thickness calibration was done by observing the conductance oscillations during the deposition of Bi on an epitaxially grown Bi(111) film on Si(111) at a substrate temperature of 12 K and then converting the result from Bi(111) bilayers (1 BL = 1.14×10^{15} atoms/cm^2) to Bi(110) bilayers (1 BL = 1.85×10^{15} atoms/cm^2 [15]). All coverages mentioned in the following refer to bilayers of Bi(110) and are average coverages, unless otherwise specified.

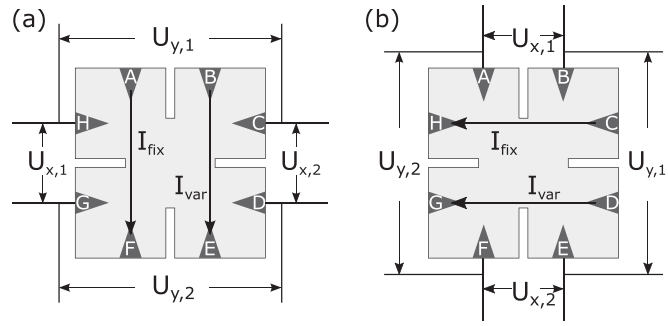

FIG. 1. Schematic of the transport measurement setup with eight contacts (A–H). See text for details.

The transport measurements were performed using a symmetrized eight-point measurement setup as shown in Fig. 1. The contacts were made directly between molybdenum clamps and the graphene layer. The slits were used to prevent crosstalk between the contacts and realized by carefully scratching the graphene layer. In order to minimize the components of the current perpendicular to the desired direction, a variable current I_{var} was applied in addition to a fixed current I_{fix} and adjusted before the measurements (at zero magnetic field) so that the voltages $U_{y,1}$ and $U_{y,2}$ were minimized. This current was then kept constant throughout the measurement. The magnetoresistivity ρ_{xx} and the Hall resistivity ρ_{xy} were determined via

$$\rho_{xx} = \gamma \frac{U_x}{I}, \quad \rho_{xy} = \frac{U_y}{I},$$

with $U_x = (U_{x,1} + U_{x,2})/2$, $U_y = (U_{y,1} + U_{y,2})/2$, $I = I_{\text{fix}} + I_{\text{var}}$, and γ being a correction factor. For a standard Hall bar, this correction factor is equal to the ratio of the contact distance for the measurement of U_y to the contact distance for the measurement of U_x. For our setup, we determined the correction factor with the help of the van der Pauw method via $\gamma = \rho_{\text{vdp}} \cdot I(B = 0)/U_x(B = 0)$, where ρ_{vdp} is the resistivity determined using the general van der Pauw formula requiring the measurement of two resistances (our sample geometry did not fulfill the symmetry condition for the simplified formula; we used the contacts A, C, E, and G) [26]. The magneto- and Hall conductivities were then determined using the tensor relations:

$$\sigma_{xx} = \frac{\rho_{xx}}{\rho_{xx}^2 + \rho_{xy}^2}, \quad \sigma_{xy} = \frac{-\rho_{xy}}{\rho_{xx}^2 + \rho_{xy}^2}.$$

By switching the voltage and current contacts two measurement directions can be realized as shown in Figs. 1(a) and 1(b). The resistivities and conductivities presented in this paper are averages of these two directions.

The LEED measurements were performed at a sample temperature of 77 K in the same UHV chamber using a SPA-LEED.

The STM measurements were performed at room temperature (RT) in a variable temperature STM (VT-STM) operating at a base pressure of 1×10^{-10} mbar. The samples for the STM measurements were prepared in the same way as for

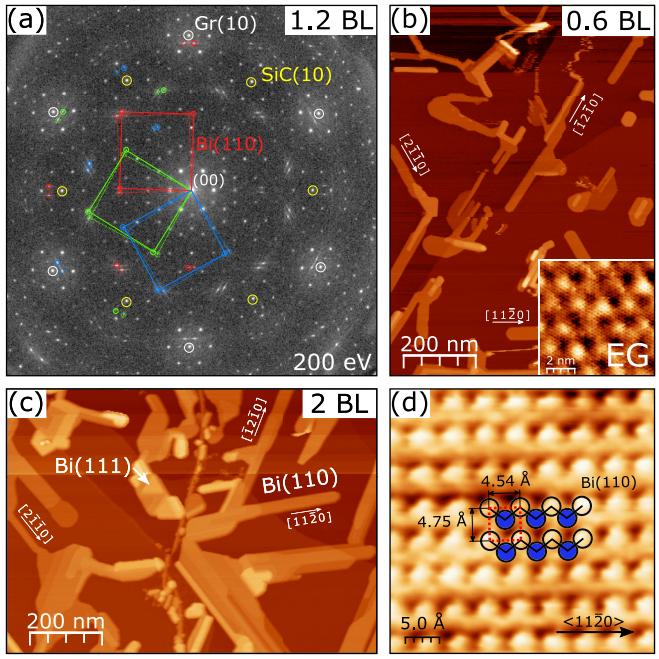

FIG. 2. (a) LEED image of MLG/SiC(0001) with a Bi coverage of 1.2 BL recorded at 200 eV. Three domains of Bi(110) are visible (red, green, and blue rectangles), each having two subdomains rotated by ±1.8° (solid and dotted lines). (b), (c) STM images for Bi coverages of 0.6 and 2 BL, respectively, showing needlelike islands. The crystallographic directions were determined from the 6 × 6 corrugation of the buffer layer shown in the inset. (d) High resolution STM scan taken on one of the needlelike islands, showing a Bi(110) surface termination. Tunneling parameters: (b) 100 mV, 200 pA; inset: 100 mV, 500 pA; (c) 100 mV, 600 pA; (d) −100 mV, 1.9 nA. Further details about the growth are reported in Ref. [16].

the magnetotransport measurements, except that 5 × 10 mm^2 wafer pieces were used.

III. RESULTS AND DISCUSSION

A. Structure of Bi(110) on MLG

Figure 2(a) shows the LEED image of MLG on SiC(0001) with a Bi coverage of 1.2 BL deposited at 300 K. From the LEED image it is clear that Bi(110) is the dominant phase of the adsorbate. Due to the symmetries involved, i.e., graphene and SiC(0001) having a hexagonal symmetry while the unit cell of the Bi(001) surface is rectangular, there are three Bi(110) domains rotated by 60° with respect to each other (red, green, and blue). Additionally, each of these domains has two subdomains rotated by approximately ±1.8° marked by solid and dotted lines, respectively, which were already observed in Ref. [15].

The STM images in Figs. 2(b) and 2(c) for coverages of 0.6 BL and 2 BL, respectively, show that the adsorbed Bi predominantly grows as needlelike islands aligned along the SiC $\langle 1\,1\,\bar{2}\,0\rangle$ directions, in line with previous STM measurements [14,17]. These islands are (110) terminated as confirmed by the STM image in Fig. 2(d). In addition, a minority of triangular Bi(111) islands are visible, e.g., in Fig. 2(c). For a more detailed analysis, see Ref. [16].

The growth mode and the epitaxial orientation as well as the azimuthal relaxation of the islands show that the Bi interacts only weakly with the substrate. This is supported by STM findings according to which, for example, Bi islands can be easily displaced laterally at high scanning speeds. Most important for the transport experiments, the STM images show that there is no percolation of the adsorbed Bi at a coverage of 0.6 BL and it only starts to develop at 2 BL.

B. Magnetotransport

The results of the magnetotransport measurements for sample 1 with Bi coverages from 0 to 3.6 BL are shown in Fig. 3. With increasing Bi coverage, a quasiparabolic contribution to the longitudinal magnetoresistivity ρ_{xx} arises, while the slope of the Hall resistivity is reduced. Without considering any quantum corrections, a homogeneous 2D free-electron gas with only one carrier type shows no magnetoresistivity, i.e., $\rho_{xx}(B) = \rho_0 = \sigma_0^{-1}$, where σ_0 is the conductivity at zero magnetic field [27]. In contrast, in the magnetoconductivity a classical contribution resulting from the elongation of the electron paths by the Lorentz force exists due to the tensor relations. The Hall resistivity measurements, shown in Fig. 3(b), remain perfectly linear at all coverages, demonstrating that only one carrier type contributes to the magnetotransport for all Bi coverages. From photoemission experiments it is known that Bi acts as an electron acceptor and dopes holes into graphene [28]. Apparently, the charge carriers in MLG are not able to penetrate into the areas below the Bi islands (see discussion below), so that even if the islands induce other carrier types, they do not affect the transport measurements. In a two-band model, a linear Hall resistivity only occurs if either one of the mobilities is very small, in which case the effect of this carrier type on the transport results is negligible or the two carrier concentrations are equal [27]. However, it is reasonable to expect that the concentration of a second carrier type induced by the islands would be much smaller than the graphene carrier concentration, especially at low Bi coverages. Therefore, the emergence of the second carrier type should result in S-shaped Hall curves. The second carrier type concentration should then also change as a function of the coverage, resulting in a different curve shape. These effects, however, are not observed. Thus the quasiparabolic contribution to the magnetoresistivity in Fig. 3(a) is not due to the emergence of a second carrier type, but instead indicates disorder or inhomogeneity in the sample. This will be discussed in Sec. III B 1. Furthermore, WL results in a sharp peak in ρ_{xx} and a dip in σ_{xx} at low fields $B < B_{\mathrm{tr}} = \hbar/(4eD\tau_{\mathrm{tr}}) \approx 50$ mT, where D is the diffusion coefficient and $\tau_{\mathrm{tr}} = h\sigma_0/(2e^2 v_F\sqrt{\pi n})$ is the transport time. For monolayer graphene $D = v_F^2\tau_{\mathrm{tr}}/2$ [20]. The WL contribution is highlighted in the inset of Fig. 3(c). The fact that it is limited to very low magnetic fields allows for it to be treated separately from other contributions, thus simplifying the analysis. The WL contribution will be discussed in detail in Sec. III B 2.

1. Effects of disorder and inhomogeneity

It was shown that additional quantum effects due to disorder induced electron-electron interaction (EEI) are important for MLG [29–31]. The EEI results in a correction $\delta\sigma_{ee}$ to

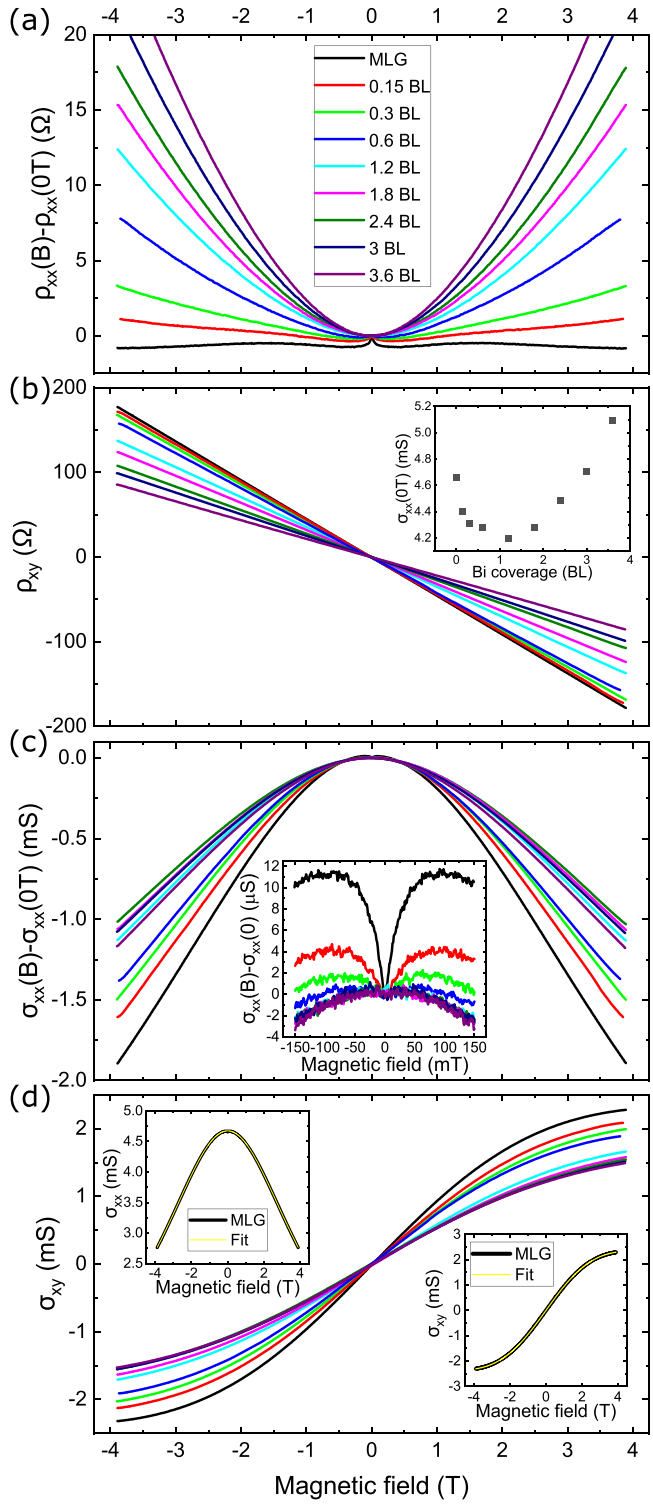

FIG. 3. Evolution of (a) the magnetoresistivity, (b) the Hall resistivity, (c) the magnetoconductivity, and (d) the Hall conductivity with increasing Bi coverage at 12 K. The insets show (b) the conductivity at zero magnetic field, (c) additional high resolution measurements of the magnetoconductivity at low fields, where the WL peak is visible, as well as (d) fits of the magnetoconductivity and the Hall conductivity for pristine graphene. The measurements were taken on sample 1.

σ_{xx}, while it does not affect σ_{xy} [32–35]. This correction is independent of the magnetic field, except for a transition at $B_Z = k_B T/(g_L \mu_B)$, with g_L being the Landé factor, due to the Zeeman splitting becoming important [36,37]. Assuming $g_L \lesssim 4$ [38], the minimal transition field is $B_Z \approx 4.5$ T, which is outside our range of measurement. Furthermore, due to the tensor relations, the EEI correction affects both ρ_{xx} and ρ_{xy}. It results in a correction $\Delta\rho_{xx} \propto -(1-\mu^2 B^2)\delta\sigma_{ee}/\sigma_0^2$ for $\delta\sigma_{ee} \ll \sigma_{xx}$ to the magnetoresistivity, as well as a change in the slope of ρ_{xy} [30]. By fitting the magnetoconductivity and Hall conductivity curves of the pristine graphene using the functions

$$\sigma_{xx} = \frac{en\mu}{1+\mu^2 B^2} + \delta\sigma_{ee}, \quad \sigma_{xy} = \frac{en\mu^2 B}{1+\mu^2 B^2},$$

respectively [see insets of Fig. 3(d)], where n is the electron concentration, μ is the mobility, and e is the elementary charge, we obtain $n = 1.39 \times 10^{13}$ cm^{-2}, $\mu = 2110$ cm^{2}V^{-1}s^{-1}, and $\delta\sigma_{ee} = -36.9$ μS. The B-dependent terms in the fitting functions are due to the classical contribution. The EEI correction $\delta\sigma_{ee}$ is related to the temperature independent Fermi liquid constant F^σ [29,32,36,39]. Our value of $\delta\sigma_{ee} = -36.9$ μS at a temperature of 12 K corresponds to $F^\sigma = -0.097$ (see the Supplemental Material for details [40]), which is in line with theoretical expectations and previous measurements [29,31]. Indeed, an increase of the EEI would result in an increase of the quasiparabolic contribution of ρ_{xx} and a decrease of the absolute value of the slope of ρ_{xy} as observed in Figs. 3(a) and 3(b), respectively. However, a classical geometric contribution due to inhomogeneous carrier concentration or mobility induced by the Bi islands also reduces the absolute Hall slope and gives rise to a parabolic contribution to ρ_{xx} at low fields $B \ll \mu^{-1}$, which transitions into a linear contribution at high fields $B \gg \mu^{-1}$ [23]. In our case $\mu^{-1} \geqslant 4.74$ T, so that a quasiparabolic contribution for $B \leqslant 4$ T would be in line with theory.

In order to clarify the origin of the quasiparabolic contribution to ρ_{xx} we performed temperature dependent magnetotransport measurements. Figure 4(a) shows $\rho_{xx}(B)$ curves at a Bi coverage of 1.2 BL and temperatures from 12 to 110 K. These measurements were performed on sample 2 ($n = 1.09 \times 10^{13}$ cm^{-2}; $\mu = 2064$ cm^{2}V^{-1}s^{-1}). While ρ_0 increases almost linearly with increasing temperature, the shape of the curves, in particular for magnetic fields over 1 T, remains essentially unchanged, which proves that the contribution is classical and due to a nonuniform sample. The Hall coefficient slightly increases with increasing temperature as seen in Fig. 4(b). In contrast to the results obtained for sample 1, the magnetoresistivity of sample 2 is already quasilinear at coverages of 1.2 and 2.4 BL and $B > 1$ T. A reasonable model to explain a linear magnetoresistivity at fields lower than the above mentioned condition of $B \gg \mu^{-1}$ is the Parish-Littlewood model [41,42]. This model predicts a linear dependence of the slope of the linear part of the magnetoresistance $\mathrm{MR} = [\rho_{xx}(B) - \rho_{xx}(0)]/\rho_{xx}(0)$ on the average mobility [25,43]. We plotted the slope of the MR between 3 and 4 T against the mobility for the temperature dependent measurements performed on sample 2 at a Bi coverage of

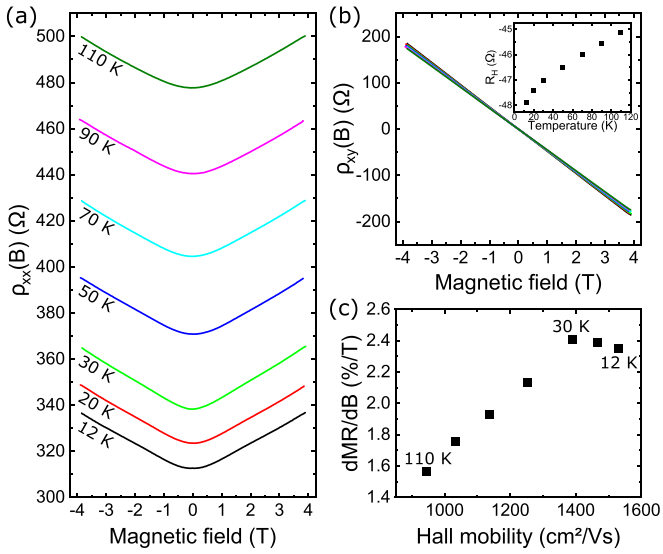

FIG. 4. (a) Magnetoresistivity and (b) Hall resistivity at different temperatures from 12 to 110 K and at a Bi coverage of 1.2 BL. Inset: corresponding Hall coefficients. (c) Slope of $MR = [\rho_{xx}(B) - \rho_{xx}(0)]/\rho_{xx}(0)$ between $B = 3$ and 4 T in dependence of the Hall mobility. The measurements were taken on sample 2.

1.2 BL in Fig. 4(c). Between 110 and 30 K the dependence is linear as expected. However, below 30 K the slope saturates indicating also a small deviation from the Parish-Littlewood model.

As stated above, nonuniformities in samples decrease the absolute value of the slope of the Hall resistivity, which leads to an overestimation of the carrier concentrations when determining it solely from the Hall resistivities [23]. In order to circumvent this problem, we determined the carrier concentration also from the Shubnikov–de Haas (SdH) oscillations, which were present in sample 2 in our range of measurement as shown in Fig. 5(a). The SdH oscillations are plotted against the inverse magnetic field in Figs. 5(c)–5(f). In order to make them clearly visible a third-order polynomial background was subtracted. The period Δ of the oscillations in these plots is directly related to the carrier concentration via

$$n_{\mathrm{SdH}} = \frac{4e}{h}\frac{1}{\Delta(1/B)},$$

where the factor 4 is due to two spin and two valley degrees of freedom in monolayer graphene [44]. The carrier concentrations determined using different methods are compared in Fig. 5(g). The coverage independence of n_{SdH} shows that the increase of the carrier concentration determined from the Hall resistivity and therefore the change of the slope of the Hall resistivity, with increasing coverage is solely due to the increasing inhomogeneity. On the other hand, the carrier concentration determined from the Hall conductivity is closer to n_{SdH}, so that in the absence of SdH oscillations it gives a better estimation of the real carrier concentration. In contrast to our magnetotransport results, angle-resolved photoemission spectroscopy measurements by Gierz *et al.* showed a comparatively strong decrease of the carrier concentration with increasing Bi coverage [28]. We compare these results to ours in Fig. 5(g). In order to understand this apparent

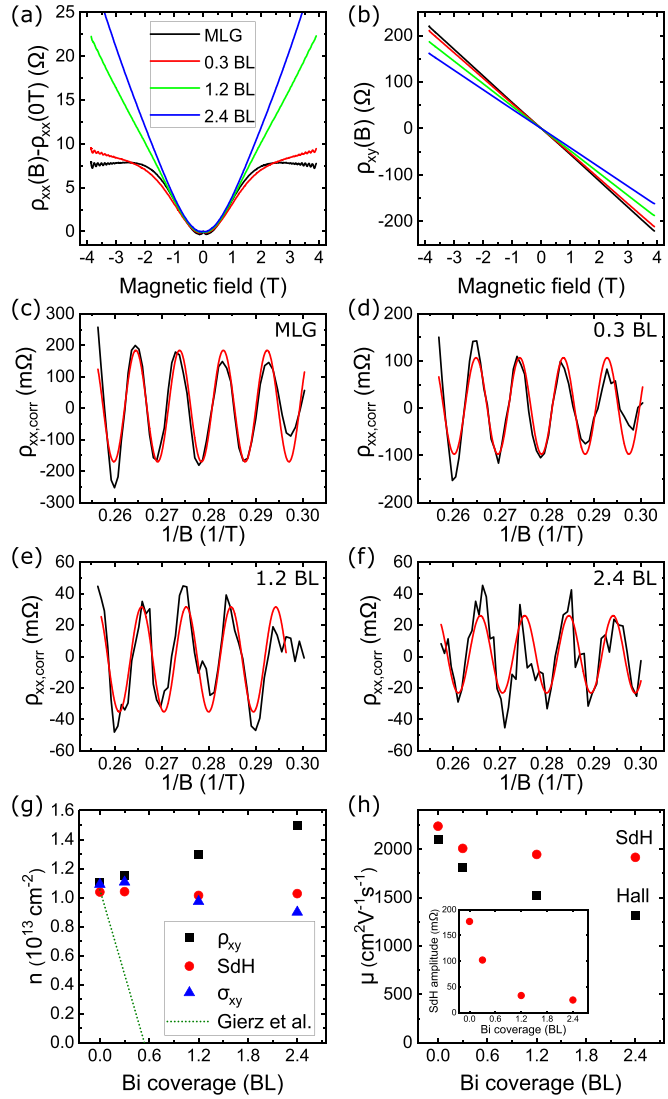

FIG. 5. (a) Magnetoresistivity and (b) Hall resistivity at different coverages at 12 K. (c)–(f) Shubnikov–de Haas (SdH) oscillations (black) with a sine fit (red) after subtraction of a third-degree polynomial background. (g) Comparison of the coverage dependence of the carrier concentration determined from the Hall resistivity, the SdH oscillations, and the Hall conductivity, as well as ARUPS measurements by Gierz *et al.* [28]. (h) Mobilities determined using the SdH and Hall carrier concentrations, respectively. Inset: amplitudes of the sine fits of the SdH oscillations. The measurements were taken on sample 2.

contradiction, one has to keep in mind that magnetotransport is only sensitive to the percolated phase, i.e., the uncovered regions [23]. Viewed as a whole, the magnetotransport and photoemission spectroscopy measurements indicate that, although Bi heavily dopes the graphene with holes, this doping is limited to the areas covered by Bi, i.e., the carrier concentration in the uncovered regions remains essentially unchanged, resulting in a highly inhomogeneous carrier concentration. This inhomogeneous charge carrier concentration is most likely indicated by the increased linewidth in the photoemission measurements. The mobilities determined using the SdH and Hall carrier concentrations, respectively, are summarized

in Fig. 5(h). These mobilities correspond to the mobilities in the uncovered region, since the potential barriers created by the Bi islands obviously do not allow the transport electrons to penetrate into the areas below the islands. The mobility as determined from the SdH oscillations decreases by less than 15% from 2240 to 1915 $cm^2V^{-1}s^{-1}$. The Hall mobility underestimates the actual carrier mobility, resulting in a larger apparent decrease [23]. The inhomogeneity increases the scattering of the electrons, which is evident from the reduction of the SdH amplitude shown in the inset of Fig. 5(h). Our findings are in agreement with models describing the islands as nonconducting zones. One such theoretical model, describing a two-dimensional electron gas with randomly distributed antidot structures, was developed by Polyakov *et al.* [24]. They describe several cases resulting in different behaviors of the magnetoresistance. In particular, our case of a positive magnetoresistance was found to be due to the presence of short-range inhomogeneities in addition to smooth disorder. It is a result of the interplay of the influence of the low conducting regions on the drift lines of the electrons and diffusive transport. A similar model that was specifically developed to explain the microscopic origin of linear magnetoresistance, which we observed in sample 2, was developed by Kozlova *et al.* [25]. Scattering events in the vicinity of low conducting islands, either due to low mobility or low carrier concentration, influence the electron trajectories in such a way that they result in a positive linear magnetoresistance above a characteristic magnetic field, that is, the inverse of the spatial average of the mobility.

2. *Weak localization*

The correction to the magnetoconductivity due to WL for MLG without SOC is given by [19,20]

$$\Delta\sigma(B) = \frac{e^2}{\pi h}\left[F\left(\frac{B}{B_\varphi}\right) - 2F\left(\frac{B}{B_\varphi + B_*}\right) - F\left(\frac{B}{B_\varphi + 2B_i}\right)\right],$$

with

$$F(z) = \ln(z) + \Psi\left(\frac{1}{2} + \frac{1}{z}\right),$$

$$B_x = \frac{\hbar c}{4De}\tau_x^{-1}, \quad x = \varphi, i, *,$$

where Ψ is the digamma function, D is the diffusion coefficient, $\tau_*^{-1} = \tau_w^{-1} + \tau_v^{-1} + \tau_i^{-1}$, τ_φ is the coherence time, i.e., the time until the phase is randomized, τ_i is the intervalley scattering time, τ_v is the intravalley scattering time, and τ_w is the trigonal warping relaxation time. Since τ_v is the dominant contribution to τ_*, the latter one is often also referred to as the intravalley scattering time.

To account for SOC, two mechanisms are generally considered: the Kane-Mele mechanism, which is intrinsic to the graphene, and the Bychkov-Rashba mechanism, which requires the $z \to -z$ symmetry to be broken due to, e.g., the substrate or adsorbates [20,22]. Both mechanisms are associated with their own characteristic scattering times. Out of these two mechanisms only the Bychkov-Rashba mechanism can induce a sharp negative peak in the resistivity (which corresponds to a positive peak in the conductivity) associated with the predominance of WAL, while the Kane-Mele mechanism merely suppresses the WL [22].

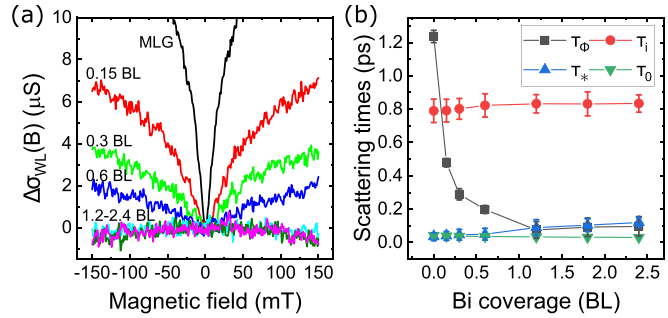

FIG. 6. (a) WL contribution to the magnetoconductivity. The classical contribution was subtracted. Cyan: 1.2 BL; magenta: 1.8 BL; olive: 2.4 BL. (b) Scattering times τ_Φ, τ_i, and τ_* determined from a fit to the data in (a) and the elastic scattering time $\tau_0 = \tau_{tr}/2$ determined from the classical contribution. $\tau_\Phi^{-1} = \tau_\varphi^{-1} + \tau_{KM}^{-1}$. The measurements were taken on sample 1.

Figure 6(a) shows the WL contribution to the magnetoconductivity at low fields. This is the same data set shown in the inset of Fig. 3(b) after subtraction of the classical contribution. With increasing Bi coverage the WL dip is more and more suppressed until it completely vanishes at 1.2 BL. The fact that there is no sign of a sharp WAL peak, even when the coverage is increased further, rules out the Bychkov-Rashba mechanism. In order to then account for the Kane-Mele mechanism, it suffices to replace τ_φ^{-1} in the above equation with a new scattering rate $\tau_\Phi^{-1} = \tau_\varphi^{-1} + \tau_{KM}^{-1}$, where τ_{KM} is the Kane-Mele scattering time [20] (see the Supplemental Material for a detailed explanation [40]). This means, however, that τ_φ and τ_{KM} are not independent fitting parameters. The scattering times obtained under these considerations from fits to the data are shown in Fig. 6(b).

The most striking feature is that τ_Φ strongly decreases with increasing Bi coverage. The question is whether this is due to a decrease of τ_φ or τ_{KM}. The Kane-Mele SOC opens a band gap $2\Delta_{KM}$ at the K point, which is related to τ_{KM} via $\tau_{KM}^{-1} = \tau_0^{-1}(\Delta_{KM}/\epsilon_F)^2$, where ϵ_F is the Fermi energy with respect to the Dirac point [20,45]. Explaining the decrease of τ_Φ with a decrease of τ_{KM} would require a band gap of $2\Delta_{KM} \approx 280$ meV at 0.15 BL and $2\Delta_{KM} \approx 880$ meV at 1.2 BL to open at the K point. This would have a significant effect on the transport characteristics. In particular, the effective mass should strongly increase, for which there is no evidence in our data. Moreover, a band gap of this magnitude should have easily been observed in angle resolved photoemission [28]. Therefore, the decrease of τ_Φ has to be caused predominantly by a decrease of τ_φ, i.e., the Bi islands introduce phase breaking scattering. The error made when equating τ_φ and τ_Φ is less than 1%, even when assuming $2\Delta_{KM} = 20$ meV, which is already at the upper end of expectations (cf. [46]).

At coverages below 1 BL, where the coherence time has not yet reached saturation, the inter- and intravalley scattering times remain constant. These measurements are, however, not sensitive to scattering events at the Bi islands for the following reasons. The coherence length $l_\varphi = \sqrt{D\tau_\varphi}$ of the noncovered graphene of approximately 250 nm corresponds to the

maximum circumference of the closed loops contributing to the WL effect. The noncovered areas in Figs. 2(b) and 2(c) are large enough, so that closed scattering loops of this size, that do not contain any scattering events at the Bi islands, still exist. Only these scattering loops contribute to the WL effect, since the scattering at the Bi islands is phase breaking, which suppresses the required quantum interference. Therefore, the effect of the islands on the inter- and intravalley scattering is not reflected in the WL effect.

IV. SUMMARY AND CONCLUSION

In summary, the epitaxial Bi islands dope the graphene only locally creating a highly inhomogeneous carrier concentration, which leads to a quasiparabolic/quasilinear contribution (depending on the details of the substrate preparation) to the magnetoresistivity. In addition, it decreases the absolute slope of the Hall resistivity, resulting in an overestimation of the carrier concentration. This effect is not to be confused with the doping due to the Bi islands, which could not be measured since the Bi islands induce potential barriers in the graphene that prevent the transport electrons from penetrating into the areas directly below the islands. Moreover, the scattering events at the islands are phase breaking, which suppresses the WL effect. Obviously, the interaction causes on the one hand a change of the charge concentration in the graphene while on the other hand the coupling is sufficiently small so that the graphene honeycomb structure is preserved, as suggested by the detailed analysis of the structure of the Bi islands [16]. The doping transition at the edge of the Bi islands appears to be perfect in the sense that the impedance mismatch of the wave function between the regions is manifested by a reflection of the propagating charge carriers, fully consistent with the above observations. While such concepts might be elaborated further to realize defined doping profiles by appropriately designed Bi nanostructures, it also shows that proximity coupling is closely related to homogeneous interfaces.

ACKNOWLEDGMENTS

We thank P. Richter (TU Chemnitz) for providing us with graphene samples. This work was supported by the Deutsche Forschungsgemeinschaft (DFG) Projects No. Te386/22-1 and No. Pi385/3-1 within the FOR5242 research unit and the Volkswagenstiftung Project No. 2112714. We also explicitly thank the reviewers who made a more consistent interpretation of the data possible by suggesting further measurements in the context of Fig. 4.

[1] E. L. Wolf, *Applications of Graphene: An Overview* (Springer, Berlin, 2014).
[2] J. Zhang, C. Triola, and E. Rossi, Proximity effect in graphene–topological-insulator heterostructures, Phys. Rev. Lett. **112**, 096802 (2014).
[3] K.-H. Jin and S.-H. Jhi, Proximity-induced giant spin-orbit interaction in epitaxial graphene on a topological insulator, Phys. Rev. B **87**, 075442 (2013).
[4] K. Zollner and J. Fabian, Heterostructures of graphene and topological insulators Bi_2Se_3, Bi_2Te_3, and Sb_2Te_3, Phys. Status Solidi B **258**, 2000081 (2021).
[5] S. Rajput, Y.-Y. Li, M. Weinert, and L. Li, Indirect interlayer bonding in graphene–topological insulator van der Waals heterostructure: Giant spin–orbit splitting of the graphene Dirac states, ACS Nano **10**, 8450 (2016).
[6] T. Wakamura, S. Guéron, and H. Bouchiat, Novel transport phenomena in graphene induced by strong spin-orbit interaction, C. R. Phys. **22**, 145 (2022).
[7] J. Balakrishnan, G. K. W. Koon, A. Avsar, Y. Ho, J. H. Lee, M. Jaiswal, S.-J. Baeck, J.-H. Ahn, A. Ferreira, M. A. Cazalilla, A. H. C. Neto, and B. Özyilmaz, Giant spin Hall effect in graphene grown by chemical vapour deposition, Nat. Commun. **5**, 4748 (2014).
[8] J. Zhou, Q. Liang, and J. Dong, Enhanced spin–orbit coupling in hydrogenated and fluorinated graphene, Carbon **48**, 1405 (2010).
[9] M. Gmitra, D. Kochan, and J. Fabian, Spin-orbit coupling in hydrogenated graphene, Phys. Rev. Lett. **110**, 246602 (2013).
[10] J. Balakrishnan, G. K. W. Koon, M. Jaiswal, A. H. C. Neto, and B. Özyilmaz, Colossal enhancement of spin–orbit coupling in weakly hydrogenated graphene, Nat. Phys. **9**, 284 (2013).
[11] Y. M. Koroteev, G. Bihlmayer, J. E. Gayone, E. V. Chulkov, S. Blügel, P. M. Echenique, and P. Hofmann, Strong spin-orbit splitting on Bi surfaces, Phys. Rev. Lett. **93**, 046403 (2004).
[12] P. Hofmann, The surfaces of bismuth: Structural and electronic properties, Prog. Surf. Sci. **81**, 191 (2006).
[13] L. Aggarwal, P. Zhu, T. L. Hughes, and V. Madhavan, Evidence for higher order topology in Bi and $Bi_{0.92}Sb_{0.08}$, Nat. Commun. **12**, 4420 (2021).
[14] K. Shen, C. Hua, Z. Liang, Y. Wang, H. Sun, J. Hu, H. Zhang, H. Li, Z. Jiang, H. Huang, P. Wang, Z. Sun, E. Wahlström, Y. Lu, and F. Song, Epitaxial growth of free-standing bismuth film on graphene embedded with nontrivial properties, ACS Appl. Electron. Mater. **1**, 1817 (2019).
[15] K. Takahashi, M. Imamura, I. Yamamoto, and J. Azuma, Thickness dependent band structure of α-bismuthene grown on epitaxial graphene, J. Phys.: Condens. Matter **34**, 235502 (2022).
[16] J. Koch, C. Ghosal, S. Sologub, and C. Tegenkamp, Morphology of Bi(110) quantum islands on epitaxial graphene, J. Phys.: Condens. Matter **36**, 065701 (2024).
[17] T. Hu, X. Hui, X. Zhang, X. Liu, D. Ma, R. Wei, K. Xu, and F. Ma, Nanostructured Bi grown on epitaxial graphene/SiC, J. Phys. Chem. Lett. **9**, 5679 (2018).
[18] Y. Lyu, S. Daneshmandi, S. Huyan, and C. Chu, Flexible atomic buckling and homogeneous edge states in few-layer Bi(110) films, Nano Res. **15**, 2374 (2022).
[19] K. Kechedzhi, E. McCann, V. I. Fal'ko, H. Suzuura, T. Ando, and B. L. Altshuler, Weak localization in monolayer and bilayer graphene, Eur. Phys. J.: Spec. Top. **148**, 39 (2007).
[20] E. McCann and V. I. Fal'ko, Weak localization and spin-orbit coupling in monolayer and bilayer graphene, in *Physics of*

Graphene, edited by H. Aoki and M. S. Dresselhaus (Springer, Cham, 2014), pp. 327–345.

[21] F. V. Tikhonenko, A. A. Kozikov, A. K. Savchenko, and R. V. Gorbachev, Transition between electron localization and antilocalization in graphene, Phys. Rev. Lett. **103**, 226801 (2009).

[22] E. McCann and V. I. Fal'ko, $z \to -z$ symmetry of spin-orbit coupling and weak localization in graphene, Phys. Rev. Lett. **108**, 166606 (2012).

[23] A. Shik, Non-uniform two-dimensional electron gas in a magnetic field, HAIT J. Sci. Eng. **1**, 470 (2004).

[24] D. G. Polyakov, F. Evers, A. D. Mirlin, and P. Wölfle, Quasiclassical magnetotransport in a random array of antidots, Phys. Rev. B **64**, 205306 (2001).

[25] N. V. Kozlova, N. Mori, O. Makarovsky, L. Eaves, Q. D. Zhuang, A. Krier, and A. Patanè, Linear magnetoresistance due to multiple-electron scattering by low-mobility islands in an inhomogeneous conductor, Nat. Commun. **3**, 1097 (2012).

[26] L. J. van der Pauw, A method of measuring the resistivity and Hall coefficient on lamellae of arbitrary shape, Philips Tech. Rev. **20**, 220 (1958).

[27] A. B. Pippard, in *Magnetoresistance in Metals*, edited by A. M. Goldman, P. V. E. McClintock, and M. Springford, Cambridge Studies in Low Temperature Physics (Cambridge University Press, Cambridge, UK, 1989).

[28] I. Gierz, C. Riedl, U. Starke, C. R. Ast, and K. Kern, Atomic hole doping of graphene, Nano Lett. **8**, 4603 (2008).

[29] A. A. Kozikov, A. K. Savchenko, B. N. Narozhny, and A. V. Shytov, Electron-electron interactions in the conductivity of graphene, Phys. Rev. B **82**, 075424 (2010).

[30] B. Jouault, B. Jabakhanji, N. Camara, W. Desrat, C. Consejo, and J. Camassel, Interplay between interferences and electron-electron interactions in epitaxial graphene, Phys. Rev. B **83**, 195417 (2011).

[31] J. Jobst, D. Waldmann, I. V. Gornyi, A. D. Mirlin, and H. B. Weber, Electron-electron interaction in the magnetoresistance of graphene, Phys. Rev. Lett. **108**, 106601 (2012).

[32] B. L. Altshuler and A. G. Aronov, Electron–electron interaction in disordered conductors, in *Electron–Electron Interactions in Disordered Systems* (Elsevier, Amsterdam, 1985), pp. 1–153.

[33] B. L. Altshuler, A. G. Aronov, and P. A. Lee, Interaction effects in disordered Fermi systems in two dimensions, Phys. Rev. Lett. **44**, 1288 (1980).

[34] G. M. Minkov, O. E. Rut, A. V. Germanenko, A. A. Sherstobitov, V. I. Shashkin, O. I. Khrykin, and V. M. Daniltsev, Quantum corrections to the conductivity in two-dimensional systems: Agreement between theory and experiment, Phys. Rev. B **64**, 235327 (2001).

[35] S. M. Girvin, M. Jonson, and P. A. Lee, Interaction effects in disordered Landau-level systems in two dimensions, Phys. Rev. B **26**, 1651 (1982).

[36] A. M. Finkel'shtein, Influence of Coulomb interaction on the properties of disordered metals, Zh. Eksp. Teor. Fiz. **84**, 168 (1983) [JETP **57**, 97 (1983)].

[37] A. M. Finkel'shtein, Metal–insulator transition in a disordered system, Zh. Eksp. Teor. Fiz. **86**, 367 (1984) [JETP **59**, 212 (1984)].

[38] A. V. Volkov, A. A. Shylau, and I. V. Zozoulenko, Interaction-induced enhancement of g factor in graphene, Phys. Rev. B **86**, 155440 (2012).

[39] A. M. Finkel'shtein, Electron liquid in disordered conductors, Sov. Sci. Rev. A Phys. **14**, 1 (1990).

[40] See Supplemental Material at http://link.aps.org/supplemental/10.1103/PhysRevB.109.235107 for the determination of the Fermi liquid constant and the inclusion of the Kane-Mele SOC in the WL equation.

[41] M. M. Parish and P. B. Littlewood, Classical magnetotransport of inhomogeneous conductors, Phys. Rev. B **72**, 094417 (2005).

[42] M. M. Parish and P. B. Littlewood, Non-saturating magnetoresistance in heavily disordered semiconductors, Nature (London) **426**, 162 (2003).

[43] S. Mallik, G. C. Ménard, G. Saïz, I. Gilmutdinov, D. Vignolles, C. Proust, A. Gloter, N. Bergeal, M. Gabay, and M. Bibes, From low-field Sondheimer oscillations to high-field very large and linear magnetoresistance in a $SrTiO_3$-based two-dimensional electron gas, Nano Lett. **22**, 65 (2022).

[44] K. S. Novoselov, A. K. Geim, S. V. Morozov, D. Jiang, M. I. Katsnelson, I. V. Grigorieva, S. V. Dubonos, and A. A. Firsov, Two-dimensional gas of massless Dirac fermions in graphene, Nature (London) **438**, 197 (2005).

[45] C. L. Kane and E. J. Mele, Quantum spin Hall effect in graphene, Phys. Rev. Lett. **95**, 226801 (2005).

[46] C. Weeks, J. Hu, J. Alicea, M. Franz, and R. Wu, Engineering a robust quantum spin Hall state in graphene via adatom deposition, Phys. Rev. X **1**, 021001 (2011).